



Title	Estimation of damping characteristics and optimization of curvilinear fiber shapes for composites fabricated by electrodeposition resin molding
Author(s)	Honda, Shinya; Takisawa, Hiraku; Takeda, Ryo; Sasaki, Katsuhiko; Katagiri, Kazuaki
Citation	Mechanics of advanced materials and structures, 30(21), 4407-4418 <a href="https://doi.org/10.1080/15376494.2022.2095063">https://doi.org/10.1080/15376494.2022.2095063</a>
Issue Date	2023
Doc URL	<a href="http://hdl.handle.net/2115/90155">http://hdl.handle.net/2115/90155</a>
Rights	This is an Accepted Manuscript of an article published by Taylor & Francis in Mechanics of advanced materials and structures on 12 Jul 2022, available online: <a href="http://www.tandfonline.com/10.1080/15376494.2022.2095063">http://www.tandfonline.com/10.1080/15376494.2022.2095063</a> .
Type	article (author version)
File Information	Damping_paper_honda_v1.pdf



[Instructions for use](#)

# **Estimation of damping characteristics and optimization of curvilinear fiber shapes for composites fabricated by electrodeposition resin molding**

Shinya Honda<sup>a</sup>, Hiraku Takisawa<sup>a</sup>, Ryo Takeda<sup>a</sup>, Katsuhiko Sasaki<sup>a</sup>,  
Kazuaki Katagiri<sup>b</sup>

*<sup>a</sup> Division of Mechanical and Aerospace Engineering, Faculty of Engineering,  
Hokkaido University, Sapporo, Japan;*

*<sup>b</sup> Research Division of Machining and Molding, Osaka Research Institute of Industrial  
Science and Technology, Osaka, Japan;*

Shinya Honda, honda@eng.hokudai.ac.jp, Division of Mechanical and Aerospace  
Engineering, Faculty of Engineering, Hokkaido University, Kita 13 Nishi 8, Kita-ku,  
Sapporo, Hokkaido, 060-8628, Japan,

# **Estimation of damping characteristics and optimization of curvilinear fiber shapes for composites fabricated by electrodeposition resin molding**

The effect of both curvilinear fiber orientation and thickness distribution on modal damping of carbon fiber reinforced plastics (CFRP) fabricated by electrodeposition resin molding (ERM) was investigated. Tailored fiber placement (TFP) was used to manufacture carbon fiber (CF) preforms with continuous curvilinear fiber paths or variable-axial properties. The damping of composites were calculated using the concept of specific damping capacity (SDC). Fiber shapes were optimized to maximize the first modal SDC using particle swarm optimization (PSO). As a result, the optimum fiber shape improves both the first natural frequency and modal SDC in comparison with several unidirectional fiber shapes.

Keywords: composite materials; tailored fiber placement; electrodeposition resin molding; vibration; damping; optimization; variable-axial stiffness;

## **1. Introduction**

Carbon fiber reinforced plastic (CFRP) is an anisotropic material whose mechanical properties depend on the orientation of carbon fibers. Recently, the development of fiber placement techniques such as automated fiber placement (AFP), tailored fiber placement (TFP), and 3D printers enabled manufacturing of continuous curved fiber shapes, which significantly extends the design freedom of the anisotropic properties of CFRP. Among these, the TFP is a technique based on embroidery machines and is suitable for mass production of relatively small structures, and in the present study it is employed to fabricate carbon fiber (CF) preforms with variable-axial properties. For resin impregnation into the preforms, an electrodeposition resin molding (ERM) method, which the authors recently proposed [1–3], is employed. The ERM is an

application of the electrodeposition technique used for automobile body coating. This is also suitable for mass production and works well with TFP handling dry CFs.

Many researchers including authors [4] studied composites with curved fiber paths and revealed the appropriate design of fiber shapes archives better mechanical characteristics to structures with straight fibers. Related to this, many of the findings are summarized in reference [5]. For example, Bittrich et al. [6] optimized fiber shapes and thickness distribution to improve the tensile properties of an open-hole plate and narrow-middle plate. Almeida et al.[7] studied the effects of curved fiber on tensile properties of an open-hole plate, and revealed curvilinear fiber shapes reduce stress concentration. Regarding dynamic properties of variable-axial composites, natural frequencies and modal shapes were studied by using the Ritz method [8] and  $p$ -version finite element analysis [9]. The authors [10] optimized the variable-axial composites to enhance the fundamental frequency, and Ikeda et al. [11] designed the fiber shapes to expand the gap between the first and second natural frequencies. In recent years, many other studies on the dynamic properties of variable-axial composites have been reported [12–16]. These studies confirmed the superiority of curved fiber shapes over straight fiber orientations.

FRP composites including CFRP have high damping characteristics mainly caused by its resin, and damping is also anisotropic. Hu et al. [17] and Pathan et al. [18] calculated the damping of CFRP using the finite element method for the plate with conventional straight fibers. Pereira et al [19], [20] investigated the effect of curved fibers on damping and the use of multi-objective optimization to maximize the fundamental modal frequency and damping. Our previous study [21] worked on vibration characteristics of CFRP with curved fibers fabricated by the ERM. In the study, we revealed the damping of CFRP by the ERM more strongly depends on fiber

shapes than those by vacuum-assisted resin transfer molding (VaRTM) due to the difference of matrix materials. However, fiber shapes were limited to simple forms such as duplication of sine curves in parallel. To take advantage of the design freedom of curved fibers, it is necessary to adopt a more flexible method of expressing the fiber shape. Moreover, the work of Pereira et al. [19,20] and the authors [10] did not consider the thickness distribution of CFRP caused by curved fiber shapes in numerical calculation. The thickness of variable-axial composite locally changes due to the overlap and gaps between fiber tows caused by curvature variation in curved fiber paths. For more accurate numerical calculation, it is important to consider the thickness distribution of CFRP.

Relating to damping calculations of CFRP with curvilinear fibers, there is no study of simultaneous application of a highly flexible fiber shape and estimation of its thickness distribution, especially for the composites fabricated by the ERM method. In the present study, we optimize fiber shape considering thickness distribution to maximize the first modal damping of CFRP fabricated by the ERM. Additionally, we conduct experimental modal analysis to evaluate both the accuracy of damping calculation and the optimization results. Damping is modeled by specific damping capacity (SDC) and calculated using finite element analysis (FEA). Damping parameters for composites fabricated by the ERM are identified using the FEA in combination with experimental modal analysis. Radial basis functions (RBFs), which are defined by linear combinations of Gaussian functions, are used to generate curvilinear fiber shapes that are defined by projecting the RBF contours onto a horizontal plane. We determine the specific fiber placement by a sequential calculation considering the overlap of CF tows, and then estimate thickness by the proposed method. As a result, it turned out that the present method accurately predicts thickness

distribution of variable-axial composites, obtained optimum fiber shapes by particle swarm optimization (PSO) improved the first modal SDC compared to some straight fibers, and validity of the numerical results were proven by the experimental results.

## 2. Damping model

### 2.1 Specific damping capacity (SDC)

The specific damping capacity (SDC) is employed to model the damping properties of plates in the present study. The SDC  $\psi$  is defined as the ratio of the dissipated energy  $\Delta U$  to the maximum strain energy  $U$  in one vibration cycle  $\psi = \Delta U / U$ . For orthotropic materials including CFRP, the SDC is calculated as

$$\psi = \frac{\sum_{i,j=1,2,3} \Delta U_{ij}}{\sum_{i,j=1,2,3} U_{ij}} = \frac{\sum_{i,j=1,2,3} \psi_{ij} U_{ij}}{\sum_{i,j=1,2,3} U_{ij}} \quad (1)$$

where  $\Delta U_{ij}$ ,  $U_{ij}$ , and  $\psi_{ij}$  are the dissipated energy, the maximum energy, and SDC in each direction of the anisotropic principal axes. This SDC is referred to as material SDC in the present paper. Strictly speaking, the material SDC is frequency-dependent, but in this study, the change is considered negligible and treated as a non-frequency-dependent parameter. Since the value of  $\psi$  calculated by the Eq. (1) is specific to each vibration mode, it is called the modal SDC to distinguish it from the material SDC. Mode SDC represents the damping of the entire structure. The material SDC in each direction was identified by comparing experimental modal analysis and FEA results of plain weave and orthogonal plate fabricated by the TFP in a preliminary experiment.

## ***2.2 Numerical calculation method for mode SDC***

The modal SDC is calculated by the following procedure [22] using ANSYS Mechanical APDL 2019 R3 and Python 3.7.5.

- (1) Run modal analysis: Assuming that the change in eigenmodes due to damping is quite small, a modal analysis (real eigenvalue analysis) was performed without considering damping to reduce computational cost.
- (2) Obtain stress and strain in the global coordinate: Stresses and strains in each element of each layer were obtained from the modal analysis results.
- (3) Transform coordinate to anisotropic principal axes: Stress and strain in the global coordinate obtained in step (2) are transformed to anisotropic principal axes using fiber orientation angle at each element in each layer.
- (4) Calculate strain energy: Strain energy in each direction of anisotropic principal axes is calculated using element volume in each layer with stress and strain obtained in step (3).
- (5) Calculate modal SDC: Modal SDC for each mode is calculated by substituting strain energy and material SDCs to Eq. (1).

## **3. Manufacture of CFRP**

### ***3.1 Fabrication of carbon preforms by TFP***

Preforms with curved fiber orientation was achieved using TFP which is an application of an embroidery machine. CF tows are fixed to the base material in an arbitrary shape by a needle and sewing thread. Figure 1 shows the lamination of carbon fiber preforms. Two layers of carbon fiber plain weave TR3110MS (Mitsubishi Chemical Corporation)

laminated in  $0^\circ$  and  $45^\circ$  directions were used as the base material, and two layers of CF tow TR50S12L (Mitsubishi Chemical Corporation) were sewn onto it using the TFP to fabricate two sets of 4-layer preforms as shown in Fig. 1 (a). By assembling these laminates on the base layer side, the 8-layer symmetrical laminate shown in Fig. 1 (b) was fabricated.

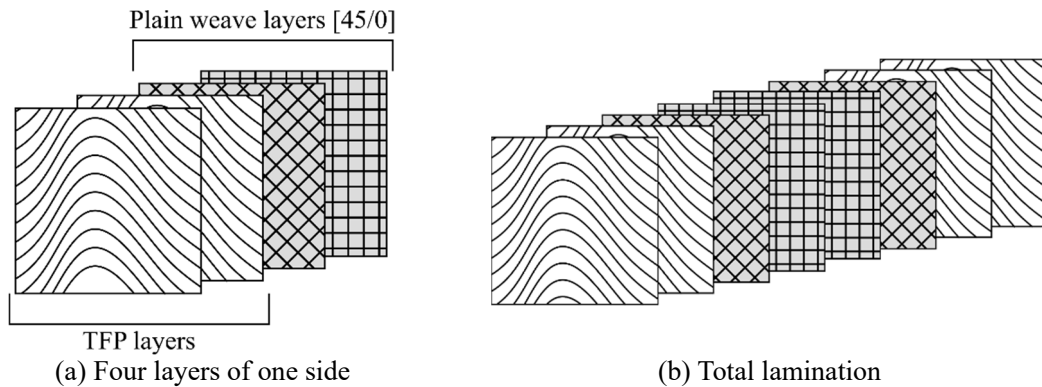


Figure 1. Lamination of CFRP with TFP layers.

### 3.2 Electrodeposition resin molding (ERM)

Figure 2 illustrates the experimental equipment for the electrodeposition resin impregnation method (ERM). The carbon fiber laminate is hanged by a metal electrode and sunk in an epoxy-containing electrolytic solution. By current application, epoxy resin is precipitated around the carbon fiber surface. That is, the CF itself acts as a cathode, and resin is deposited more homogeneously on each fiber than other methods of injecting resin by physical pressure [2]. Figure 3 is a schematic diagram of resin precipitation, showing the gradual deposition and growth of resin from the surface of the carbon fiber. Elecoat AR (Shimizu Co., Ltd.) was used as the electrodeposition solution. As the resin impregnation progresses by current flow, the resistance of the cathode (preform) increases, and thus the voltage decreases for a given current according to Ohm's law.



After resin impregnation, excess electrodeposition liquid and voids remaining inside the preform were removed using a press machine and vacuum desiccator. The two preforms were assembled on the base layer side, sandwiched between PTFE sheets and silicon mats, and heat-cured under pressure using metal plates and vises.

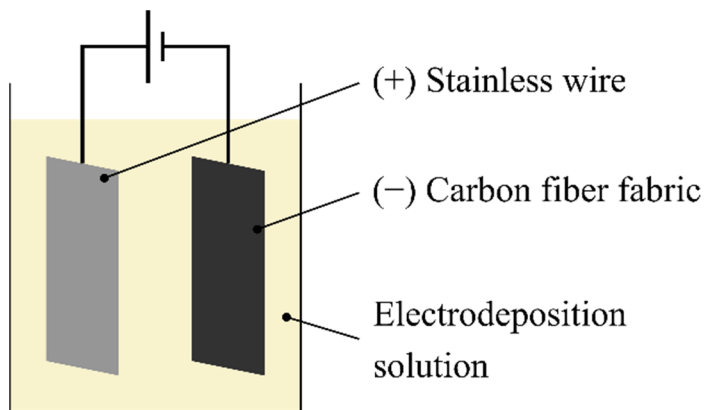


Figure 2. Experimental equipment for ERM.

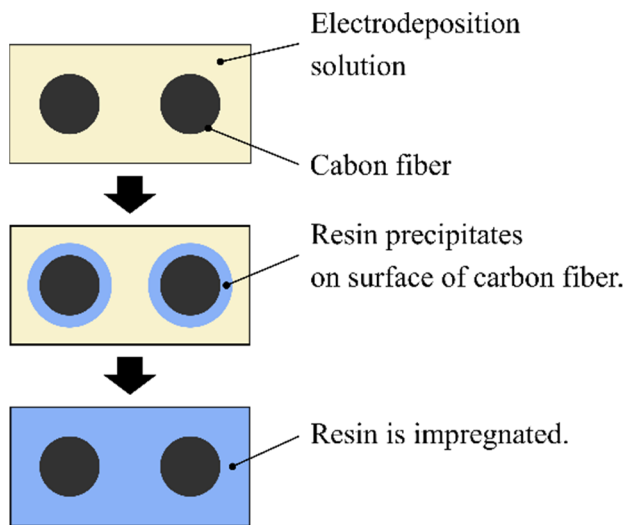


Figure 3. Schematic diagram of resin impregnation in ERM.

## 4. Curved fiber shapes and thickness distribution

### 4.1 Expression of curvilinear fiber paths by contour lines

In this study, the contour lines of the surface are treated as paths of fibers to represent curvilinear fiber orientation. To create the fiber shape with a high degree of freedom, a linear combination of radial basis functions (RBFs) was used to define the surface. The RBF is a function whose value depends only on the distance from a point. The surface function  $f(x, y)$  defined by the RBF is given by the following equation. Three Gaussian functions are employed to represent the surfaces.

$$f(x, y) = \sum_{i=1}^3 w_i \exp \left( -\frac{(x - x_{c,i})^2 + (y - y_{c,i})^2}{r_i^2} \right) \quad (2)$$

Here,  $x_{c,i}$ ,  $y_{c,i}$  and  $r_i$  ( $i = 1, 2, 3$ ) are the parameters for Gaussian functions, and  $w_i$  ( $i = 1, 2, 3$ ) are the weight factors. A single Gaussian function gives a concentric fiber shape, but a linear combination of multiple Gaussians can represent a fiber shape with a high degree of freedom.

It is difficult to apply the continuous fiber orientation defined by contour lines directly to finite elements. Therefore, the fiber shape was discretized for each element of the finite element model and treated as a straight fiber within each element. The fiber orientation angle  $\theta_e$  in the  $e$ th element is equal to the inclination of the tangent to the contour line at the center of the  $e$ th element  $(x_e, y_e)$ , and it is calculated as follows.

$$\theta_e = \tan^{-1} \left( -\frac{\partial f / \partial x}{\partial f / \partial y} \right) \Big|_{(x,y)=(x_e,y_e)} \quad (3)$$

Regardless of the scale, it is easier to deal with a one-to-one correspondence between the parameters that define the surface and the fiber shape. Therefore, the fiber shape was calculated within a region normalized by the length of the lower edge of the plate.

Figure 4 indicates (a) the example of a curved surface, (b) projected contour lines on the horizontal surface, and (c) fiber orientation discretized for the FEA model.

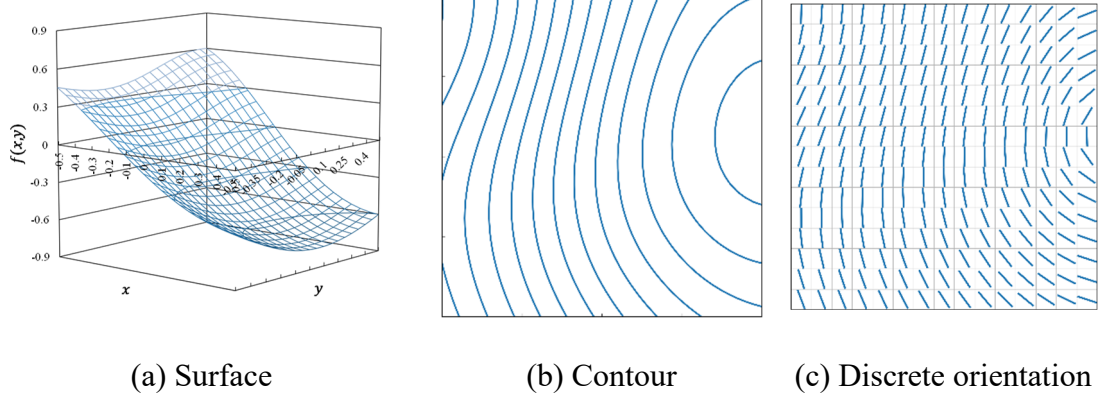


Figure 4. Example of a surface defined by Eq. (2) with the corresponding contour and discretized fiber shape.

#### 4.2 Fiber placement for TFP fabrication

To fabricate preforms using TFP, it is necessary to determine the specific arrangement of the fiber tows that provide the path for stitching. On the other hand, there are countless ways to draw contour lines on a curved surface, depending on the spacing between them. Therefore, the width of the fiber tows was used as a constraint to control the spacing of the contour lines and to determine the arrangement of the fiber tows. The overlap ratio  $\alpha$  as a measure of the degree of overlap, which is defined as the ratio of the width of the overlap to the width of the fiber bundle, is introduced as follows.

$$\alpha = \frac{w_f - d}{w_f} \quad (4)$$

Here,  $w_f$  is the width of the fiber tow and  $d$  is the distance between the center lines of adjacent fiber tows. From Eq. (4), the distance  $d$  between adjacent fiber bundles is determined if the overlap ratio  $\alpha$  at a certain point is given. In this paper, the maximum

overlap ratio was specified as  $\alpha_{\max}$ , and the minimum distance between adjacent fiber bundles was determined as  $d_{\min} = (1 - \alpha_{\max})w_f$ . The arrangement of the contour lines that satisfied this minimum distance was determined by sequential calculations, and it was used as the arrangement of the carbon fiber tows for preform fabrication. The following are the procedure of the fiber placement calculation, and Fig. 5 shows a schematic diagram of the procedure. Note that this procedure can be applied to any function  $f(x, y)$  which defines a curved surface with Eq. (2).

- (1) Generate the calculation grid: Set up a computational grid to calculate the passing points of the contour lines. In consideration of the layer thickness estimation, the grid was made twice as fine as the meshing of the FEA.
- (2) Calculate  $z_i = f(x_i, y_i)$ : The value of  $f$  is calculated at the reference point of the  $i$ th fiber  $(x_i, y_i)$  ( $i = 1, 2, 3, \dots$ ). The reference point here is a point for determining the contour line. The reference point for the first fiber is selected arbitrarily.
- (3) Calculate the passing points of the  $i$ th fiber bundle: To find the set of points passing through the  $i$ th contour line,  $(x, y)$  satisfying  $f(x, y) = z_i$  is calculated on the computational grid. For this calculation,  $x$  (or  $y$ ) is fixed and corresponding  $y$  (or  $x$ ) needs to be searched. The solution cannot be obtained analytically when the linear combination of Gaussian functions defined in Eq. (2) is used as  $f(x, y)$ . Here, the solution is calculated using the false position method, which always finds a solution and converges faster than the bisection method.
- (4) Search the maximum gradient point  $(X_i, Y_i)$ : On the  $i$ th contour line, compare the gradient  $|\nabla f|$  at each passing point, and find the point  $(X_i, Y_i)$  ( $i = 1, 2, 3, \dots$ ) with the maximum gradient since the distance between adjacent

contour lines in front and behind becomes the narrowest at the point with the maximum gradient. If the overlap ratio at this point is set to the maximum value  $\alpha_{\max}$ , the minimum distance between adjacent contour lines is calculated as  $d_{\min} = (1 - \alpha_{\max})w_f$  according to Eq. (4).

- (5) Update the reference point: The point  $d_{\min}$  away from the point  $(X_i, Y_i)$  in the normal direction of the contour line is selected as the next reference point  $(x_{i+1}, y_{i+1})$  on the  $i + 1$  contour line. The new point is calculated as follows.

$$\begin{aligned} (x_{i+1}, y_{i+1}) &= (X_i, Y_i) + d_{\min} \cdot \frac{\nabla f}{|\nabla f|} \Big|_{(x,y)=(X_i,Y_i)} \\ &= (X_i, Y_i) + (1 - \alpha_{\max})w_f \cdot \frac{\nabla f}{|\nabla f|} \Big|_{(x,y)=(X_i,Y_i)} \end{aligned} \quad (5)$$

- (6) Repetition and termination condition: Steps (3)-(5) are repeated and the calculation is terminated when it is no longer possible to draw new contours within the calculation area.

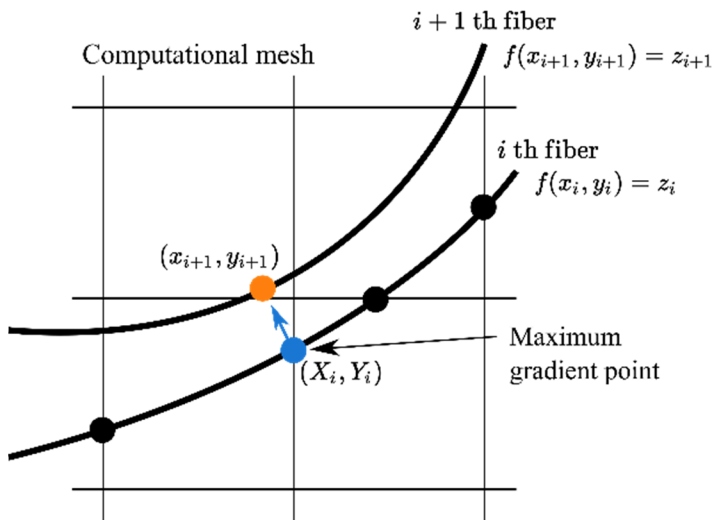


Figure 5. Schematic diagram of fiber path calculation.

### 4.3 Estimation of thickness distribution

This section describes how to estimate the thickness distribution for an arbitrary fiber shape function  $f(x, y)$ . As mentioned above, the thickness distribution occurs due to overlaps and gaps between curved fiber tows. The objective here is to express the thickness  $t$  at point  $(x, y)$  for arbitrary fiber shape function of  $f(x, y)$ . First, the relationship between the overlap ratio and the thickness is derived. Figure 6 (a) shows fiber tows lined up in a region of width  $l$  with an overlap ratio of 0, and the number of fiber tows is  $n_0 = l/w_f$ . Next, consider the situation shown in Fig. 6 (b), where the fiber tows are lined up in a region of width  $l$  with an overlap ratio of  $\alpha$ . In this case, the number of fibers  $n_\alpha$  is obtained as follows.

$$\begin{aligned} w_f + (1 - \alpha)w_f \cdot (n_\alpha - 1) &= l \\ \therefore n_\alpha &= \frac{l/w_f - \alpha}{1 - \alpha} \end{aligned} \quad (6)$$

When the thickness of the fiber bundle is  $t_f$ , the thickness of the plate at zero overlap ratio becomes  $t_f$ . Defining the plate thickness  $t$  with an overlap ratio  $\alpha$  as the average thickness in infinite width,  $t$  is obtained from the ratio of  $n_0$  and  $n_\alpha$  by the following equation.

$$t = \lim_{l \rightarrow \infty} \frac{n_0}{n_\alpha} t_f = \lim_{l \rightarrow \infty} \frac{1 - \alpha \cdot w_f/l}{1 - \alpha} t_f = \frac{t_f}{1 - \alpha} \quad (7)$$

Now the relationship between the overlap ratio  $\alpha$  and the thickness  $t$  is obtained. Using Eq. (7), the local thickness at any point is calculated using the overlap ratio  $\alpha$ . Since the distance between adjacent fiber tows and the magnitude of the gradient are inversely proportional, the space between fiber tows  $d(x, y)$  is calculated as follows.

$$d(x, y) = \frac{|\nabla f|_{\max}}{|\nabla f|_{(x,y)}} d_{\min} = \frac{|\nabla f|_{\max}}{|\nabla f|_{(x,y)}} (1 - \alpha_{\max}) w_f \quad (8)$$

Here,  $|\nabla f|_{\max}$  is the magnitude of the gradient at the point where the distance between fiber tows is the smallest on each contour line, and  $|\nabla f|_{(x,y)}$  is the magnitude of the gradient at point  $(x, y)$ . Substituting  $d(x, y)$  into Eq. (4), we can obtain the overlap ratio  $\alpha(x, y)$ .

$$\alpha(x, y) = 1 - \frac{|\nabla f|_{\max}}{|\nabla f|_{(x,y)}} (1 - \alpha_{\max}) \quad (9)$$

Substituting Eq. (9) into Eq. (7), the thickness  $t(x, y)$  can be expressed using the magnitude of the gradient of the fiber shape function  $f(x, y)$  as follows.

$$t(x, y) = \frac{|\nabla f|_{(x,y)}}{|\nabla f|_{\max}} \frac{t_f}{1 - \alpha_{\max}} = \frac{|\nabla f|_{(x,y)}}{|\nabla f|_{\max}} t_{\max} \quad (10)$$

Here,  $t_{\max}$  is the thickness at the point where the overlap ratio is the maximum on each fiber, that is, the maximum thickness. Thickness at each passing point of fiber tows is calculated by Eq. (10), and then the average thickness is calculated at each element for FEA using the grid point within the element.

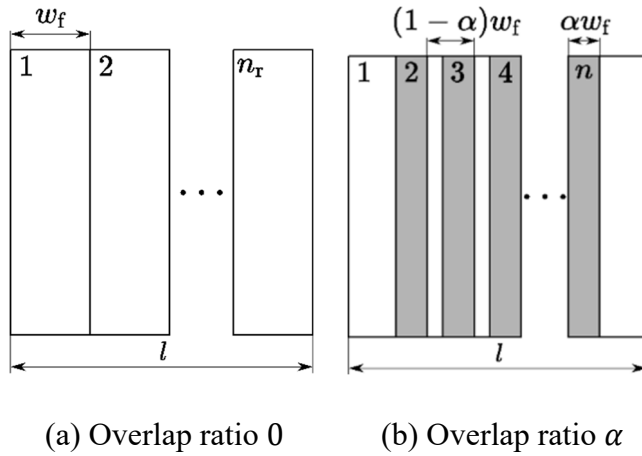


Figure 6. Schematic diagrams of fiber placement.

## 5 Fiber shape optimization

### 5.1 Optimization condition

The optimization of curved fiber orientation is performed to maximize the first modal damping  $\psi_1$ . To take advantage of the curved fiber shape, the optimization target is not a simple rectangle, but a L-shape as shown in Fig. 7 under the totally free boundary condition. As indicated in Fig. 1, the lay-up configuration was  $[(TFP)_2/PW\ 45/PW\ 0]_s$ , and the fiber shape of the TFP layers is optimized here. The design variables are the parameters of the Gaussian functions in the fiber shape function defined by Eq. (2). The objective function is the inverse of the first modal SDC  $\psi_1$ , and the parameters that minimize it are searched.

$$\begin{aligned} \text{Minimize:} \quad & f(x_{c,i}, y_{c,i}, \sigma_i, w_i) = \psi_1^{-1} \quad (i = 1, 2, 3) \\ \text{Such that:} \quad & -2 \leq x_{c,i} \leq 2, \quad -2 \leq y_{c,i} \leq 2, \\ & 0.001 \leq r_i \leq 4, \quad -2 \leq w_i \leq 2 \end{aligned} \tag{11}$$

PSO with the nonlinear dissipative term [23] is used as the optimization algorithm, and this algorithm defines the weight of inertia by nonlinear functions, while conventional PSO uses the constant value for the weight of inertia. The parameters for PSO with nonlinear dissipative term were  $c_1 = 1.4, c_2 = 1.4, d_0 = 3.0, d_1 = 0.5, d_2 = 0.02$ . Both numbers of particles and iterations were set to 200. For comparison, optimum parabolic and sinusoidal fiber shapes, and various unidirectional (UD) fibers were employed. The thickness of the laminated materials and the material constants are shown in Table 1. The material SDCs  $\psi_{ij} (i, j = 1, 2, 3)$  shown in Table 1 were identified by experimental modal analysis and FEA in preliminary experiments.



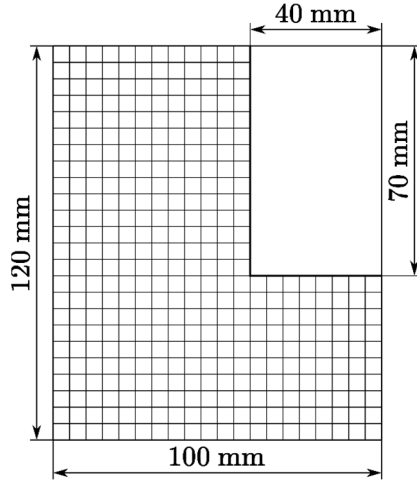


Figure 7. Dimensions of the L-shaped plate model.

Table 1. Material constants for plain weave sheet and TFP layer used in optimization.

	Thickness [mm]	$E_{11}$ [GPa]	$E_{22}$ [GPa]	$G_{12}$ [GPa]	$\nu_{12}$ [—]	$\rho$ [kg/m <sup>3</sup> ]	$\psi_{11}$ [%]	$\psi_{22}$ [%]	$\psi_{12}$ [%]
PW	0.289	37.7	37.7	3.26	0.3	1442	3.08	3.08	23.9
TFP	Variable	102.7	9.04	5.05	0.3	1295	5.19	13.5	16.4

## 5.2 Optimization results

Figure 8 shows the optimum fiber shape, thickness distribution in the TFP (sewn fiber) layers, and the first modal shape obtained by the optimization. Table 2 shows the Gaussian function parameters for the optimum fiber shape. It is known from Fig. 8(c) that the first mode shape is torsional deformation. This is because  $\psi_{12}$  which is related to shear deformation is the largest among the directional components of the material SDC. Figures 9 and 10 show the optimum parabolic and sinusoidal fiber shapes and thickness distributions. The shapes are obtained by the similar optimization method, using amplitude and frequency as design variables in the case of a sinusoidal function, and vertex point and proportionality constant in the case of a parabola. For both cases, only one fiber shape is optimized and the same fibers are placed in parallel within the

region. The ranges of the color bars in the thickness distribution are in the same range as Fig. 8(c).

Table 3 shows the first modal SDC and natural frequency for the various fiber shapes including unidirectional (UD) fibers. The thickness of the TFP layers for the UD fibers was set to 0.518 mm, which is the same as the average thickness for the optimum fiber shape shown in Fig. 8 (b). UD 4 and UD 76 in Table 3 are the unidirectional orientation angles that give the maximum and minimum first modal SDC respectively.

The optimum fiber shape by the Gaussian functions has the highest first modal SDC and natural frequency in all fiber shapes. The first mode SDC of optimum fiber shape is +9% larger than that of UD 4, which has the largest first mode SDC in UD orientations, and +36% larger than that of UD 76, which has the smallest first mode SDC. The fiber shapes obtained by optimization and UD -45 look similar, but the first modal SDC of the former is +28% higher. The first mode SDCs for the parabolic and sinusoidal fiber shapes are lower than those obtained in the optimization but higher than those for the UD orientation. These results confirm that the curved orientation is more effective to improve damping than the unidirectional orientation.

Comparing the three types of curvilinear fiber shapes, the fiber shape defined by the Gaussian functions indicates the slightly higher first modal SDC than the parabolic and sinusoidal shapes. This is because the optimum fiber shape under the present conditions is close to straight lines as shown in Figure 8 (a), and similar shapes is reproduced by parabolic and sinusoidal curves. However, when comparing the thickness distributions, the parabolic and sinusoidal fiber shapes resulted in more flat distributions than the Gaussian shape. This high degree of freedom regarding thickness distribution contributed to the higher damping of the Gaussian shape compared to other shapes. The average thickness of the TFP layer is 0.518 mm, 0.554 mm, and 0.569 mm for the

Gaussian, parabolic, and sinusoidal fiber shapes, respectively. These results imply that the Gaussian fiber shape achieves higher damping performance even with fewer materials. The optimal fiber shape has the highest frequency, although the frequency was not included in the objective function.

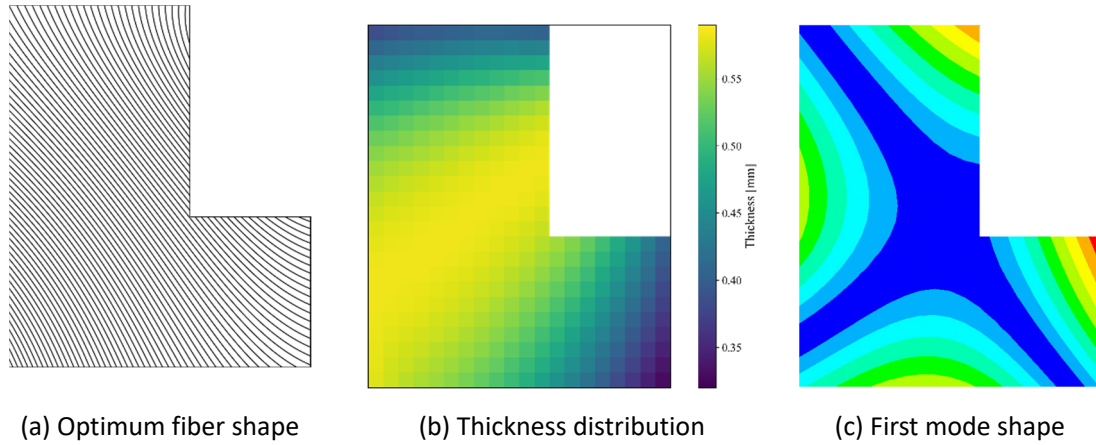
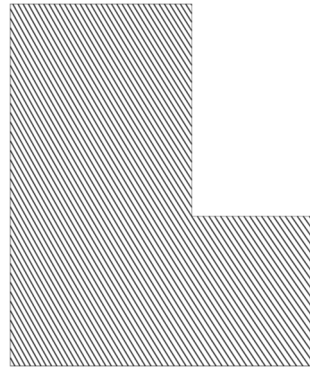


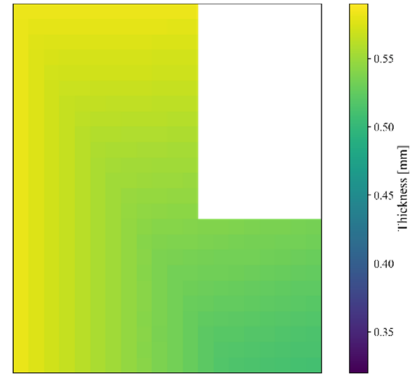
Figure 8. Obtained optimum fiber shape defined by Gaussian functions, its thickness distribution and first mode shape with the maximum first modal SDC.

Table 2. Parameters for Gaussian functions corresponding to optimum fiber shape.

$i$	$x_{c,i}$	$y_{c,i}$	$r_i$	$w_i$
1	-1.026	-0.700	0.918	-1.017
2	0.701	0.165	3.682	1.876
3	-0.592	0.587	3.992	1.102

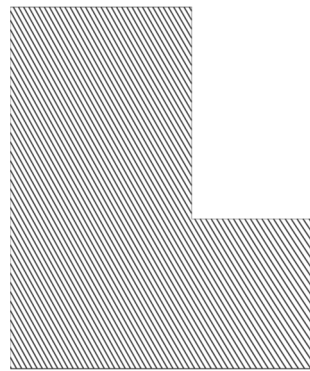


(a) Optimum fiber shape

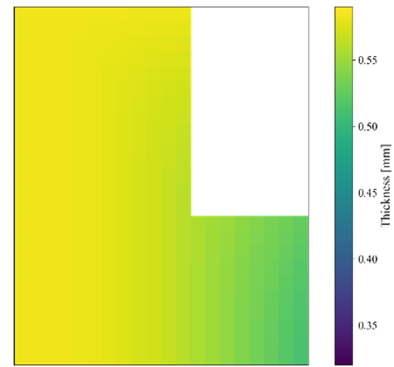


(b) Thickness distribution

Figure 9. Optimum parabola fiber shape and its thickness distribution with the maximum first modal SDC.



(a) Optimum fiber shape



(b) Thickness distribution

Figure 10. Optimum sinusoidal fiber shape and its thickness distribution with the maximum first modal SDC.

Table 3. First natural frequencies and modal SDCs calculated with curved and unidirectional (UD) fiber shapes.

Fiber shape	1 <sup>st</sup> frequency [Hz]	1 <sup>st</sup> SDC [%]
Gaussian functions (best)	757	15.6
Parabola (best)	701	15.3
Sine curve (best)	716	15.4
UD 0	676	14.3
UD 4 (best)	673	14.3
UD 45	648	12.9
UD 76 (worst)	592	11.5
UD 90	586	11.8
UD -45	683	12.2

## 6. Experimental verification

### 6.1 Fabrication of CFRP

To confirm the accuracy of the calculation for the thickness and damping, we fabricated a CFRP plate with the shape shown in Fig. 8 (a) by the TFP with ERM and conducted the experimental modal analysis. The lamination of the CFRP is [(Opt.)<sub>2</sub>/PW 45/PW 0]<sub>s</sub>, which has the optimum fiber shape defined by Eq. (2) and the parameters shown in Table 2. The current and voltage conditions for the ERM were 1.5 A constant until the voltage reaches 200 V, and constant 200 V is kept until current becomes less than 0.4 A. Heat curing conditions were as follows: the temperature was raised to 215°C in 2 hours, then kept in an oven for 6 hours, and cooled at room temperature. Table 4 shows the material constants used in FEA for comparison. Note that these data differ from those

shown in Table 1 because, as a result of trial and error, new conditions were applied that allowed for a more efficient manufacturing process by the ERM.

Table 4. Material constants for plain weave sheet and TFP layer used in comparison.

	Thickness	$E_{11}$	$E_{22}$	$G_{12}$	$\nu_{12}$	$\rho$	$\psi_{11}$	$\psi_{22}$	$\psi_{12}$
	[mm]	[GPa]	[GPa]	[GPa]	[–]	[kg/m <sup>3</sup> ]	[%]	[%]	[%]
PW	0.184	37.7	37.7	3.26	0.3	1442	6.14	6.14	29.4
TFP	Variable	102.7	4.80	3.20	0.3	1295	3.01	20.1	22.5

## 6.2 Measurement of thickness distribution

To confirm the accuracy of the thickness calculation, the thickness distribution of the fabricated plate with optimum fiber shape is measured. Since the thickness distribution described above did not include pressure during thermal curing, a correction factor for thickness is needed for accurate estimation and it is calculated based on the experimental results. First, the thicknesses of 91 points were measured by using a micrometer, and the result is shown in Fig. 11 (a). The blank space in the figure is the area where the micrometer could not reach. The average thickness of the plate was 2.51 mm. With this result, the thickness of the fiber bundle was set to 0.30 mm so that the average value of the calculated thickness distribution would agree with the result.

Figure 11 (b) shows the thickness distribution calculated using the determined fiber tow thickness. The ranges of the color bars are the same in Fig. 11 (a) and (b). From these two thickness distributions, it can be said that the trends of both distributions are consistent. However, the difference between the thin and thick areas is larger in the estimated distribution than those measured. Fig. 11 (c) is the distribution of

the difference between the measured and estimated value. The difference is calculated as  $(\text{exp.} - \text{calc.})/\text{exp.} \times 100 [\%]$ . In Fig. 11 (c), the measured thickness is thicker than the estimated value in red areas and thinner in the blue areas.

Comparing Fig. 11 (b) and Fig. 11 (c), the thickness is underestimated in the lower right and upper area, while it is overestimated near the center where the estimated thickness is large. The first and second lines in Table 5 show the mean value, maximum value, minimum value, and standard deviation (SD) of the distributions obtained by measurement and numerical calculation. The measured thickness distribution gives small values of both the SD and the range between minimum and maximum. These results show that the calculation overestimates the dispersion of the thickness. The reason for this is that the compression during the curing process was not considered. The uneven laminated material was sandwiched between flat metal plates during heat curing, and the thicker areas were highly pressurized while the thinner areas were only lightly pressurised. Thus, resulting in a thickness distribution with little dispersion for the fabricated plate.

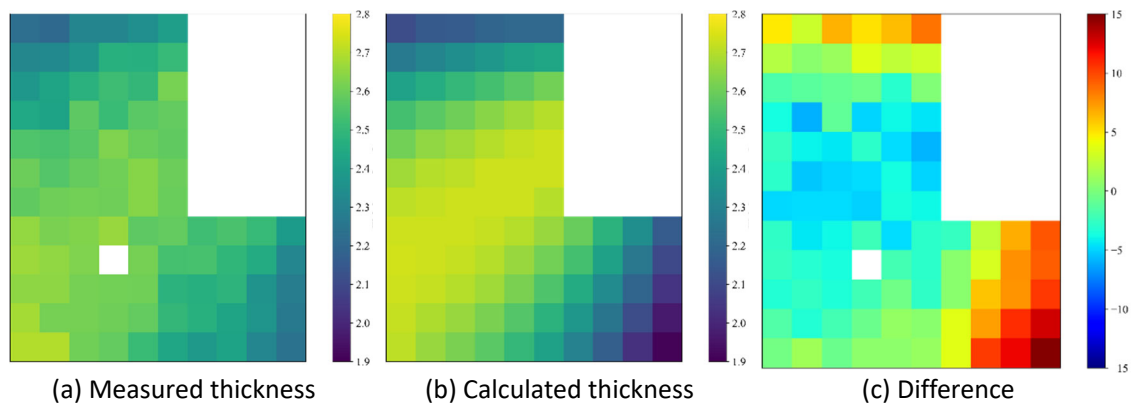


Figure 11. Thickness distribution measured and calculated with fiber. tow thickness of 0.30 mm and those differences.

Table 5. Thickness distribution obtained by experiment and calculation.

	Thickness [mm]			
	Average	Max.	Min.	SD
Measured	2.51	2.70	2.21	0.120
Calc.without correction	2.51	2.74	1.91	0.223
Calc. with correction	2.51	2.63	2.18	0.121

It is necessary to decrease the dispersion of the thickness in the calculation for a more accurate estimation. Therefore, the thickness correction is applied using the following equation.

$$t'_{\text{calc}} = t_{\text{calc}} + \frac{t_{\text{ave}} - t_{\text{calc}}}{c} \quad (12)$$

Here,  $t_{\text{calc}}$  and  $t'_{\text{calc}}$  is the calculated thickness before and after the correction respectively, and  $t_{\text{ave}}$  is the average of the measured thickness.  $c$  is the correction factor, and as the value approaches 1, the dispersion of the corrected thickness becomes small. When  $c = 1$ ,  $t'_{\text{calc}}$  is equal to  $t_{\text{ave}}$ , and this correction does not change the average thickness regardless of the value of  $c$ . As a result of trial and error, we found the SD of the estimated thickness distribution agrees with that of the measured one when  $c = 2.2$ .

Figure 12 (a) is the thickness distribution corrected using the correction factor, and Fig. 12 (b) shows its difference from the measured value shown in Fig. 11 (a). The range of the color bar is unified among Fig. 11 (a), Fig. 11 (b), and Fig. 12 (a) and between Fig. 11 (c) and Fig. 12 (b). The last line in Table 5 lists the corrected thickness



distributions. The difference decreased greatly by the correction, and the difference of the minimum value, which was particularly large before the correction, also improved. This validates the effectiveness of the correction defined by Eq. (12). In the next section, this correction is applied to the numerical analysis.

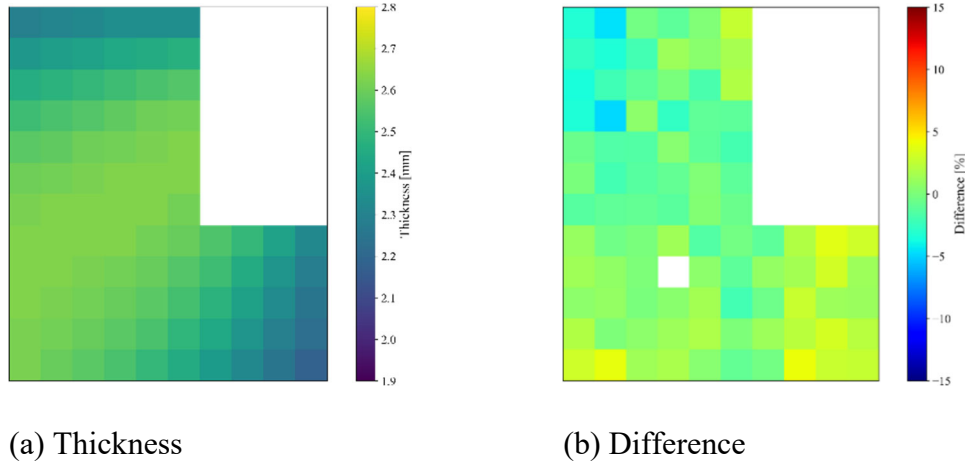


Figure 12. Corrected thickness distribution calculated with fiber thickness of 0.30 mm and thickness collection factor.

### 6.3 Experimental modal analysis

64 grid points on the fabricated composite plate were excited five times respectively by an impulse hammer. The dimensions and material constants shown in Table 4 were used in the numerical analysis for comparison. Figures 13 and 14 show the mode shapes and natural frequencies obtained from the experiment and FEA, and the modal SDCs and difference between experiment and calculation, which are defined by  $\text{diff.} = (\text{exp.} - \text{calc.}) / \text{exp.} \times 100 [\%]$ . The second mode obtained numerically could not be clearly obtained experimentally. This might be caused by the fact that the second frequency is very close to the first.

As for the natural frequencies, the experimental values are lower than the calculated values for all modes. The difference for the first mode that is the objective of

the optimization is 4% between the experimental and calculated results, showing good agreement. However, the experiment gives more than  $-20\%$  lower values for the third and fourth modes. This is because the reduction of the elastic modulus due to the gap of fiber tows is not included in the calculation. On the other hand, regarding the modal SDC, the experimental values agree well with the calculated values from the first to third modes. Although there is a relatively large difference in the fourth mode, the trend of the modal SDC transition agrees between the experimental and calculated values. This result shows that the present calculation method successfully evaluates the modal damping for CFRPs fabricated by the ERM. The reason for the large difference in the higher mode is that the material SDC was identified by using only the lower modes.

Finally, the effect of applying thickness distribution to the FEA was investigated. Figure 15 indicates The first mode shapes, frequencies, and modal damping obtained by (1) experiment, (2) FEA with estimated thickness distribution, and (3) FEA with constant thickness. In the case of (3), the thickness of the TFP layer was set to 0.444 mm so that the total thickness of the eight layers coincides with the measured average thickness of 2.51 mm. The first natural frequency does not change largely by applying the thickness distribution. However, the thickness distribution affects the first mode shape and modal SDC significantly, and the difference to the experimental results is much larger without thickness distribution. Therefore, it can be concluded that the estimation of the thickness distribution is extremely important for predicting modal damping by numerical calculation.

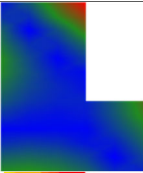
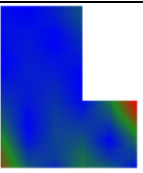
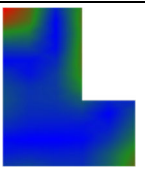
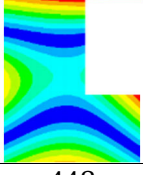

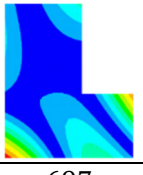
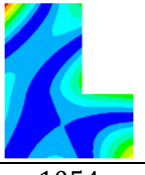
Mode No.		1 <sup>st</sup>	2 <sup>nd</sup>	3 <sup>rd</sup>	4 <sup>th</sup>
Mode shape	Exp.		—		
	FEA				
Frequency [Hz]	Exp.	448	—	697	1054
	FEA	466	476	848	1285
	Diff. [%]	-4.0	—	-21.7	-22.0

Figure 13. Measured and calculated mode shapes and natural frequencies.

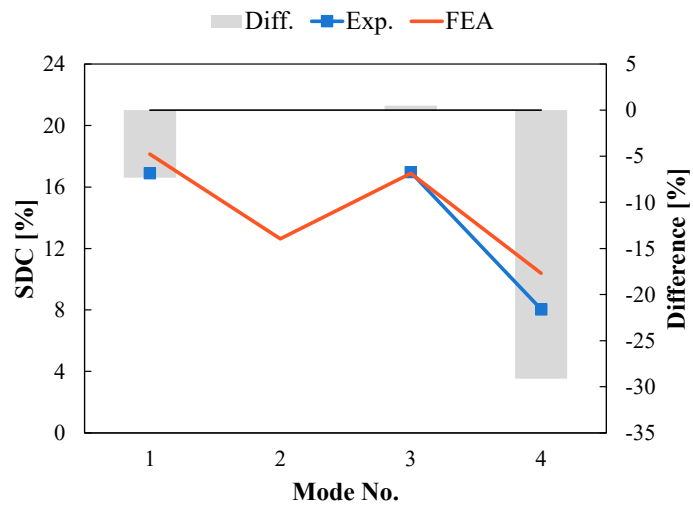


Figure 14. Measured and calculated mode SDCs and their differences.

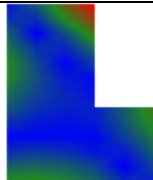
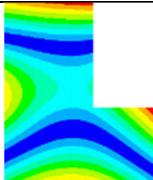
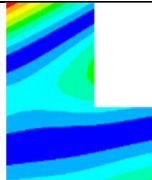
	Exp.	FEA with variable thickness	FEA with constant thickness
Mode shape			
Frequency [Hz]	448	466	426
SDC [%]	16.8	17.9	9.9

Figure 15. The first frequencies and mode shapes obtained by the experiment and FEA with two types of thickness configuration.

## 7. Conclusion

In this study, the specific damping capacity (SDC) was estimated numerically, and the fiber shape was optimized to maximize the first modal SDC for composites assuming the fabrication of the electrodeposition resin molding (ERM). For the test specimen fabricated by the tailored fiber placement (TFP) machine and the ERM, the experimental modal analysis was conducted to evaluate the results of numerical analysis and optimization. The fiber shape was expressed by contour lines of a surface defined by a linear combination of Gaussian functions or radial base function (RBF), which generates flexible fiber shapes. The thickness distribution caused by curved fiber shapes was estimated and applied to the finite element analysis.

To validate the optimization result, unidirectional (UD) fiber shapes and two types of optimum curved fiber shapes, parabolic and sinusoidal curves, were employed for comparison. The optimum results had the highest first natural frequency and modal

SDC, in addition the optimum parabolic and sinusoidal curves, and UD  $-45$  plates had a similar shape to the optimum curved fiber. These results implies that the present flexible expression method for curved fiber shapes is effective for improving damping of composites. The present thickness estimation and optimum distributions for curved fiber shapes also demonstrated that the flexible fiber shape achieve higher damping with less materials. This implies that the present fiber shape expression is more useful when the plate shape and conditions are more complex.

The test specimen with the optimum fiber shapes defined by the Gaussian functions was fabricated for the experiments to verify the analysis results. The results of the experimental modal analysis indicate that the trend of modal SDCs is estimated numerically for CFRPs with curved fiber shapes fabricated by the ERM. It was also examined that the effect of thickness distribution on numerical damping calculation by comparing three results: the experimental results, FEA with thickness distribution, and FEA without thickness distribution. The first mode shapes and SDC differed greatly from the experimental results when the thickness distribution was not applied. This result concludes that the estimation of thickness distribution is important to calculate damping for CFRPs with curved fiber shapes.

### **Declaration of interests**

The authors declare that they have no known competing financial interests or personal relationships that could have appeared to influence the work reported in this paper.

### **Author's contribution**

Shinya Honda: Conceptualization, Funding acquisition, Project administration, Writing

- original draft; Hiraku Takisawa: Data analysis, Numerical calculation, Experiment, Writing - original draft; Ryo Takeda: Writing – review & editing; Katsuhiko Sasaki: Katsuhiko Sasaki: Supervision; Kazuaki Katagiri: Writing – review, Supervision.

## **Funding**

This work was supported by JSPS KAKENHI Grant Number 20H02094.

## **Reference**

- [1] Katagiri K, Honda S, Nakaya S, Kimura T, Yamaguchi S, Sonomura H, et al. Tensile strength of CFRP with curvilinearly arranged carbon fiber along the principal stress direction fabricated by the electrodeposition resin molding. *Composites Part A: Applied Science and Manufacturing* 2021;143.  
<https://doi.org/10.1016/j.compositesa.2021.106271>.
- [2] Katagiri K, Sasaki K, Honda S, Nakashima H, Yamaguchi S, Ozaki T, et al. CFRP manufacturing method using electrodeposition resin molding for curvilinear fiber arrangements. *Composites Part A* 2017;102:108–16.  
<https://doi.org/10.1016/j.compositesa.2017.07.006>.
- [3] Katagiri K, Sasaki K, Honda S, Nakashima H, Tomizawa Y, Yamaguchi S, et al. Resin molding by using electro-activated deposition for efficient manufacturing of carbon fiber reinforced plastic. *Composite Structures* 2017;182:666–73.  
<https://doi.org/10.1016/j.compstruct.2017.09.064>.

- [4] Honda S, Igarashi T, Narita Y. Multi-objective optimization of curvilinear fiber shapes for laminated composite plates by using NSGA-II. *Composites Part B: Engineering* 2013;45:1071–8. <https://doi.org/10.1016/j.compositesb.2012.07.056>.
- [5] Lozano GG, Tiwari A, Turner C, Astwood S. A review on design for manufacture of variable stiffness composite laminates. *Proceedings of the Institution of Mechanical Engineers, Part B: Journal of Engineering Manufacture* 2015. <https://doi.org/10.1177/0954405415600012>.
- [6] Bittrich L, Spickenheuer A, Almeida JHS, Müller S, Kroll L, Heinrich G. Optimizing Variable-Axial Fiber-Reinforced Composite Laminates: The Direct Fiber Path Optimization Concept. *Mathematical Problems in Engineering* 2019;2019. <https://doi.org/10.1155/2019/8260563>.
- [7] Almeida JHS, Bittrich L, Jansen E, Tita V, Spickenheuer A. Buckling optimization of composite cylinders for axial compression: A design methodology considering a variable-axial fiber layout. *Composite Structures* 2019;222:110928. <https://doi.org/10.1016/j.compstruct.2019.110928>.
- [8] Honda S, Narita Y. Natural frequencies and vibration modes of laminated composite plates reinforced with arbitrary curvilinear fiber shape paths. *Journal of Sound and Vibration* 2012;331:180–91. <https://doi.org/10.1016/j.jsv.2011.08.019>.
- [9] Akhavan H, Ribeiro P. Natural modes of vibration of variable stiffness composite laminates with curvilinear fibers. *Composite Structures* 2011;93:3040–7. <https://doi.org/10.1016/J.COMPSTRUCT.2011.04.027>.
- [10] Honda S, Narita Y. Vibration design of laminated fibrous composite plates with local anisotropy induced by short fibers and curvilinear fibers. *Composite Structures* 2011;93:902–10. <https://doi.org/10.1016/j.compstruct.2010.07.003>.

- [11] Ikeda T, Oka K, Nishida T. EIGEN-FREQUENCY CONTROL DESIGN OF CFRP STRUCTURES USING AN EMBROIDERY MACHINE. In: First International Symposium on Flutter and its Application, editor., Minato-Ku, Tokyo, Japan: Japan Aerospace Exploration Agency (JAXA); 2017, p. 111–20.
- [12] Yan CA, Vescovini R, Jansen EL. A semi-analytical framework for nonlinear vibration analysis of variable stiffness plates. *Composite Structures* 2021;269:113954.  
<https://doi.org/10.1016/J.COMPSTRUCT.2021.113954>.
- [13] Yan Y, Liu B, Xing Y, Carrera E, Pagani A. Free vibration analysis of variable stiffness composite laminated beams and plates by novel hierarchical differential quadrature finite elements. *Composite Structures* 2021;274:114364.  
<https://doi.org/10.1016/J.COMPSTRUCT.2021.114364>.
- [14] Sharma N, Swain PK, Maiti DK, Singh BN. Static and free vibration analyses and dynamic control of smart variable stiffness laminated composite plate with delamination. *Composite Structures* 2022;280:114793.  
<https://doi.org/10.1016/J.COMPSTRUCT.2021.114793>.
- [15] Farsadi T, Rahmanian M, Kurtaran H. Nonlinear lay-up optimization of variable stiffness composite skew and taper cylindrical panels in free vibration. *Composite Structures* 2021;262:113629. <https://doi.org/10.1016/J.COMPSTRUCT.2021.113629>.
- [16] Venkatachari A, Natarajan S, Ganapathi M. Variable stiffness laminated composite shells – Free vibration characteristics based on higher-order structural theory. *Composite Structures* 2018;188:407–14.  
<https://doi.org/10.1016/J.COMPSTRUCT.2018.01.025>.
- [17] Hu BG, Dokainish MA. Damped vibrations of laminated composite plates— Modeling and finite element analysis. *Finite Elements in Analysis and Design* 1993;15:103–24.  
[https://doi.org/10.1016/0168-874X\(93\)90059-Y](https://doi.org/10.1016/0168-874X(93)90059-Y).



- [18] Pathan M v., Patsias S, Tagarielli VL. A real-coded genetic algorithm for optimizing the damping response of composite laminates. *Computers & Structures* 2018;198:51–60.  
<https://doi.org/10.1016/J.COMPSTRUC.2018.01.005>.
- [19] Pereira DA, Guimarães TAM, Resende HB, Rade DA. Numerical and experimental analyses of modal frequency and damping in tow-steered CFRP laminates. *Composite Structures* 2020;244:112190. <https://doi.org/10.1016/J.COMPSTRUCT.2020.112190>.
- [20] Pereira DA, Sales TP, Rade DA. Multi-objective frequency and damping optimization of tow-steered composite laminates. *Composite Structures* 2021;256:112932.  
<https://doi.org/10.1016/J.COMPSTRUCT.2020.112932>.
- [21] Takisawa H, Hashimoto N, Honda S, Katagiri K, Sasaki K, Takeda R. Vibration characteristics of carbon fiber reinforced composites fabricated by electrodeposition molding method. In: *The 15th International Conference on Motion and Vibration(MoViC 2020)*, editor., The Japan Society of Mechanical Engineers; 2020.
- [22] Yang J, Xiong J, Ma L, Wang B, Zhang G, Wu L. Vibration and damping characteristics of hybrid carbon fiber composite pyramidal truss sandwich panels with viscoelastic layers. *Composite Structures* 2013;106:570–80.  
<https://doi.org/10.1016/J.COMPSTRUCT.2013.07.015>.
- [23] Murata H, Yasuda K, Aiyoshi E. Proposal of particle swarm optimization methods with nonlinear dissipative term. *Electronics and Communications in Japan* 2008;91:23–30.  
<https://doi.org/10.1002/ecj.10028>.